Asymmetric Generation of Acoustic Vortex Using Dual-Layer Metasurfaces

Yangyang Fu,[1,2,*] Yuan Tian,[3] Xiao Li,[1,2] Shili Yang,[3] Youwen Liu,[1,2] Yadong Xu,[4,†] and Minghui Lu[3,‡]
[1]Department of Applied Physics, Nanjing University of Aeronautics and Astronautics, Nanjing 211106, China
[2]Key Laboratory of Aerospace Information Materials and Physics (NUAA), MIIT, Nanjing 211106, China
[3]National Laboratory of Solid State Microstructures and Department of Materials Science and Engineering, Nanjing University, Nanjing 210093, China
[4]School of Physical Science and Technology and Institute of Theoretical and Applied Physics, Soochow University, Suzhou 215006, China

(Received 15 June 2021; revised 12 November 2021; accepted 18 February 2022; published 9 March 2022)

In this Letter, we introduce a new paradigm for achieving robust asymmetric generation of acoustic vortex field through dual-layer metasurfaces by controlling their intrinsic topologic charges and the parity of geometry design. The underlying physics is contributed to the one-way process of orbital angular momentum (OAM) transition ensured by the broken spatial symmetry and the external topologic charge from the vortex diffraction. We further experimentally demonstrate this novel phenomenon. Our findings could provide new routes to manipulate the asymmetric response of vortex fields, including one-way excitation and propagation, and promise potential applications in passive OAM-based diodes.

DOI: 10.1103/PhysRevLett.128.104501

Asymmetric wave propagation has attracted significant interest due to its fundamental importance in many applications with one-way performance [1–4]. Many schemes in recent years have been proposed to realize optical or acoustic asymmetric effects [5–15], including magneto-optical materials [5], nonlinearity [6,7], non-Hermitian modulation [8,9], topological insulators [10,11], and metasurfaces [12–15], which leads to numerous phenomena, e.g., one-way mode conversion [16], asymmetric diffraction [17], and unidirectional excitation of surface plasmon polaritons [18]. However, previously reported efforts are almost limited to the low-freedom planar wave fields (e.g., plane waves), which are greatly challenged by these complex structured fields with higher degree of freedom, such as vortex beams with orbital angular momentum (OAM).

Since the discovery of OAM carried by waves, vortex fields have been widely studied because vortex fields with OAM offer unique opportunities to realize numerous interesting phenomena and promising applications [19] beyond the trivial plane waves, including vortex tweezers [20,21], optical microscopy imaging [22] and high-capacity communications [23,24]. Among these vortex-based studies, the generation of vortex fields is a fundamental issue, which has been widely investigated [25], particularly in the field of phase gradient metasurfaces (PGMs) [26–32]. PGMs are associated with intrinsic topological charge (ITC, denoted as l^{ξ}) to create the effect of a twisting phase, which is essentially the conventional conversion of topological charge, i.e., $l^{r(t)} = l^{\text{in}} + l^{\xi}$, where $l^{r(t)}$ and l^{in} are topological charges of the reflected (transmitted) vortex and the incident vortex, respectively. Although great progress has been made in optical or acoustic vortex generation with metasurfaces, how to generate vortex fields with highly asymmetric responses is still an open question. The exploration of asymmetric vortex generation and propagation is significant for realizing new asymmetric effects and OAM-based applications [19].

In this Letter, we theoretically propose and experimentally demonstrate, for the first time, asymmetric generation of acoustic vortex through dual-layer PGMs with different ITCs. Recently, acoustic vortex diffraction law has been proposed in a cylindrical waveguide with a single PGM [33], which enables an external topologic charge (ETC) induced by multiple internal reflections [34–36] to manipulate vortex fields in a more flexible way. By employing this additional degree of freedom in the PGM, we will reveal how the dual-layer PGMs are implemented to break the conventional conversion of topological charge and produce extremely asymmetric generation of acoustic vortex fields. The underlying physics is contributed to the one-way process of OAM transition ensured by the broken spatial symmetry and the vortex diffraction law. One PGM, engineered with the reflected ETC, blocks back the incoming plane wave from one side to forbid the OAM transition, which generates a low-efficiency acoustic vortex. While for the incidence from the opposite side, the effective combination of ITC and ETC in the two PGMs allows the OAM transition, leading to the vortex generation with high efficiency. Distinguished from previous works, this asymmetric effect could be manifested by not only the one-way transmission efficiency but different OAM states. Thanks to the robust ETC, which is physically guaranteed by the parity design of the cell number in the PGM, the

revealed asymmetric feature is also robust, making it difficult to realize with the common method that only involves the twisting phase elements, e.g., spiral phase plates. Our work, therefore, provides an effective way for asymmetric vortex generation using the dual-layer metastructures.

Figure 1(a) schematically shows the proposed concept for the asymmetric generation of acoustic vortex. It is a cylindrical waveguide consisting of two PGMs with the same thickness of h but different ITCs. The radius of the waveguide is R, and there are finite vortex modes at a fixed working frequency, with the maximum topological charge denoted as l^M. It implies that the topological charge of the propagating vortex mode survived in the waveguide belongs to $[-l^M, l^M]$, where the sign of "+" ("−") defines the clockwise (counterclockwise) helicity. The acoustic pressure field of each propagating vortex mode in the waveguide is expressed as

$$p = J_l(k_{l,\nu}r)/J_l(k_{l,\nu}R)\exp(il\theta + ik_z z), \quad \text{with} \quad -l^M \le l \le l^M, \tag{1}$$

where $k_{l,v}$ and k_z are the transverse and longitudinal wave vectors, respectively, l is the topological charge (OAM order), $k_0 = 2\pi/\lambda$ is the wave vector in air, $1/J_l(k_{l,\nu}R)$ is a normalized factor, $\partial J_{l,\nu}(k_{l,\nu}r)/\partial(k_{l,\nu}r)|_{r=R} = 0$, and $k_{l,\nu}^2 + k_z^2 = k_0^2$. The PGM-1 and the PGM-2 provide ITCs of l_1^ξ and l_2^ξ, respectively, and they are realized by l_1^ξ and l_2^ξ groups of fanlike supercells whose azimuthal phase distribution covers 2π [33]. The phase distribution of 2π over the supercell is discretized and realized by multiple unit cells. The number of these discretized unit cells in the PGM-1 (PGM-2) is denoted as m_1 (m_2), and the phase

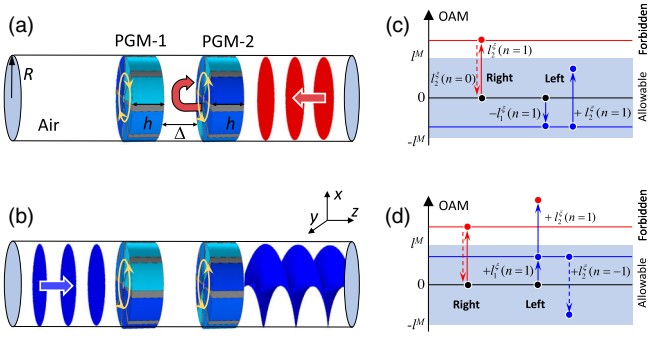

FIG. 1. Concept of asymmetric generation of acoustic vortex. Schematic diagram of a cylindrical waveguide with the dual-layer PGMs, which support the low-efficiency (a) and high-efficiency (b) generation of acoustic vortex for the left and right incidences, respectively. The physics process of asymmetric generation of acoustic vortex for the dual-layer PGMs with the opposite helicity (c) and the same helicity (d), respectively. In the plots, the solid (dashed) arrow denotes the process of ITC of the twisting phase (ETC of the vortex diffraction), and the red (blue) circle represents the forbidden (allowable) vortex mode in the waveguide.

difference of two adjacent unit cells in each supercell is $\Delta\phi = 2\pi/m_{1(2)}$. For the sake of discussion, we set $l_2^\xi > l_1^\xi > 0$ in this work.

First, let us examine the physical condition of generating a low-efficiency acoustic vortex for the incidence from the right side of the waveguide [see Fig. 1(a)]. Considering the incoming wave $l^{\text{in}} = 0$, it is twisted by the PGM-2 into a vortex mode with l_2^ξ. If $l_2^\xi > l^M$, this vortex mode is forbidden in the waveguide [see the red solid arrow in Fig. 1(c)], because its longitudinal wave vector becomes an imaginary number. As a result, multiple internal reflections [34–36] with the propagation number L happen inside the PGM-2. Consequently, the scattering vortex mode diffracted from the PGM-2 follows the diffraction law [33], i.e.,

$$\begin{cases} l^t & = l^{\text{in}} + nl_2^\xi, \quad L = \text{odd} \\ -l^r & = l^{\text{in}} + nl_2^\xi, \quad L = \text{even}, \end{cases} \tag{2}$$

where $l^{r(t)}$ is the topological charge of the reflected (transmitted) vortex, n is the diffraction order, and $L = m_2 + n$. Note that the diffraction order in Eq. (2) is higher order, belonging to $n \le 0$, because $n = 1$ is the lowest diffraction order corresponding to the conventional conversion of topological charge. If the higher diffraction order is taken, the PGM-2 can provide an equivalent ETC of nl_2^ξ. As $l_2^\xi > l^M$ and $l^{\text{in}} = 0$, the higher diffraction order of $n = 0$ is available to obtain a propagating guided mode. For the PGM-2 designed with an even number of unit cells, i.e., m_2 is even, the even propagation number of $L = m_2$ happens in the PGM-2. Then, the incident wave is blocked back with $l^r = 0$ [see the red dashed arrow in Fig. 1(c)] owing to the reflected ETC in the PGM-2 with even unit cells. In fact, this ETC, physically guaranteed by the parity design [36] of the cell number in the PGM, is very robust to block the incoming wave [37]. In this case, the low-efficiency vortex generation can happen on its transmitted side by involving the PGM-1 [see Fig. 1(a)].

Moreover, based on the condition of $l_2^\xi > l^M$ and $m_2 =$ even, let us reveal the condition of generating a high-efficiency vortex for the left incidence [see Fig. 1(b)]. Two different cases are considered; i.e., two PGMs are laid with the opposite or same helicity, as indicated, respectively, by a pair of yellow circles with arrows in Figs. 1(a) and 1(b). For PGMs with the opposite helicity, e.g., ITCs of the PGM-1 and the PGM-2 are $-l_1^\xi$ and l_2^ξ, the direct process of the twisting phase is the most convenient way to generate a high-efficiency vortex, as schematically illustrated in Fig. 1(c). The left incidence with $l^{\text{in}} = 0$ is first twisted by the PGM-1 into a vortex with $l^t = -l_1^\xi$ and then twisted by the PGM-2 into another vortex with $l^t = -l_1^\xi + l_2^\xi$ [see the blue solid arrows in Fig. 1(c)]. When the converted vortex modes are both allowable in the waveguide,

i.e.,$l_1^\xi \le l^M$ and $-l_1^\xi + l_2^\xi \le l^M$, a high-efficiency vortex with $l^t = l_2^\xi - l_1^\xi$ is generated on the right side. While for PGMs with the same helicity (l_1^ξ and l_2^ξ), the physical mechanism for high-efficiency vortex generation is different from that in the case of the opposite helicity. After the left incidence is twisted by the PGM-1 into a vortex with $l^t = l_1^\xi \le l^M$, it cannot be twisted again by the PGM-2 due to $l^t = l_2^\xi + l_1^\xi > l^M$ [see the blue solid arrow with red circle in Fig. 1(d)]. However, instead of the twisting phase effect from $n = 1$, the PGM-2 can provide the ETC of $-l_2^\xi$ via the higher diffraction order of $n = -1$. As $m_2 =$ even, $L = m_2 - 1$ is an odd number, the diffracted vortex is a transmitted one with $l^t = l_1^\xi - l_2^\xi$ [see the blue dashed arrow in Fig. 1(d)], which is an allowable OAM for $|l^t| \le l^M$.

These physical processes could be qualitatively described by overlying the corresponding transmission efficiency of OAM transition. For two opposite incidences without OAM, i.e., $\psi_{\text{in}} = [1, 1]$, the corresponding transmitted vortex fields are approximately

$$T_L = t_1 t_2 \exp[+i(\sigma l_1^\xi + n l_2^\xi)\theta], \tag{3a}$$

$$T_R = \delta_2 \delta_1 \exp[-i(\sigma l_1^\xi + n l_2^\xi)\theta], \tag{3b}$$

where t_1 and t_2 (δ_1 and δ_2) are the corresponding transmission coefficients of OAM transition through the PGM-1 and the PGM-2 for the left (right) incidence. $\sigma = -1$ and 1 represent the cases of two PGMs with the opposite and same helicity, respectively. For the left incidence, $n = 1$ ($n = -1$) is for the opposite (same) helicity, while it is $n = 0$ for the right incidence. Both cases of helicity follow the same condition, i.e., $l_1^\xi \le l^M < l_2^\xi \le l^M + l_1^\xi$ and $m_2 =$ even. The diffraction law of Eq. (2) enables $|t_1| = |\delta_1| \approx 1$ for plane waves passing through the PGM-1 from both sides. Because of the broken spatial symmetry from the PGMs with different ITCs, the PGM-2 can serve as a one-way mirror, i.e., $|t_2| \approx 1$ for the left incidence and $|\delta_2| \approx 0$ for the right incidence, to achieve asymmetric vortex generation. Therefore, by implementing the dual-layer metasurfaces in a cylindrical waveguide, asymmetric generation of acoustic vortex could be realized, which is manifested by not only unidirectional transmission efficiency but different OAM states tailored by ITCs. Note that these results are difficult to realize with the conventional way that only involves the twisting phase elements [25], e.g., spiral phase plates, as they cannot provide robust ETCs to achieve the one-way OAM transition [37].

To demonstrate the above theory, we take the case of $l^M = l_1^\xi = l_2^\xi/2 = 1$ and $m_2 = 4$ for illustration. We set $R = 0.4\lambda$ to obtain $l^M = 1$ and the working wavelength is $\lambda = 10.0$ cm. As $m_2 = 4$ and $l_2^\xi = 2$, the angular width of the fanlike unit cells in the PGM-2 is $\vartheta_2 = 360°/m_2 l_2^\xi = 45°$. The fanlike unit cell [see Fig. 2(a)] is designed by rotating its azimuthal section [Fig. 2(b)] along the z axis with $\vartheta_2 = 45°$, and the azimuthal section is

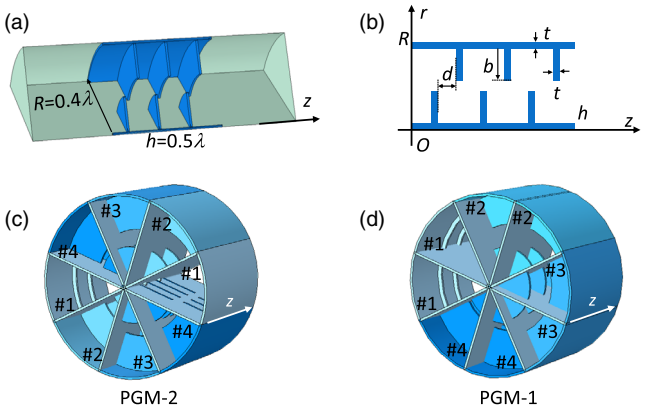

FIG. 2. PGM design. (a) Fanlike unit cell design in a fanlike waveguide. (b) Azimuthal section of a fanlike unit cell. Topography of the designed PGM-2 (c) and PGM-1 (d), where they are both constructed from four different fanlike unit cells.

designed using the coiling-up space structure [38]. The transmission and phase parameters of the fanlike unit cell are tested in a fanlike waveguide, as shown in Fig. 2(a). By changing the number, length, and space of the building blocks, four fanlike unit cells are designed to achieve the required phase profile ($\Delta\phi = \pi/2$) and nearly unity transmission [37]. The PGM-2 is designed by assembling these four unit cells [see Fig. 2(c)], which can provide the ITC of $l_2^\xi = 2$ for the incident wave propagating along the $+z$ direction. For the PGM-1, the angular width of its fanlike unit cell is $\vartheta_1 = 360°/m_1 l_1^\xi$. A similar process could be performed to obtain the PGM-1 by designing m_1 groups of unit cells. However, here we provide a neat way to directly design a PGM-1 in which new unit cells are not needed anymore. Owing to $l_2^\xi = 2l_1^\xi$, the angular width of the fanlike unit cells in the PGM-1 is $\vartheta_1 = 2\vartheta_2$ for $m_1 = 4$. Therefore, the fanlike unit cell of the PGM-1 is implemented by placing twice the corresponding unit cell of the PGM-2. Conveniently, the PGM-1 is designed [see Fig. 2(d)], and the PGM-1 provides the ITC of $l_1^\xi = -1$ as its phase gradient is opposite that in the PGM-2 (see the gradient color). A similar design principle could be extended to other dual-layer or multilayer metasurfaces [39,40], as long as their unit cells have an integral-multiple relationship. By appropriately implementing these unit cells, the PGMs could be constructed with different properties, which could enable multifunctional manipulation on vortex fields.

Based on the designed metasurfaces, we perform numerical simulations using COMSOL to verify the proposed asymmetric generation of acoustic vortex. When the dual-layer metasurfaces are placed with the opposite helicity, the corresponding simulated results are shown in Fig. 3(a). For the left incidence [see the upper plot of Fig. 3(a)], the incident plane wave is twisted into an acoustic vortex with $l = -1$ in the air gap ($\Delta = \lambda$) between the PGMs and then it is twisted again into a vortex with $l^t = -1 + 2 = 1$ on the transmitted side. However, for the right incidence [see the lower plot of Fig. 3(a)], the incident wave is almost blocked

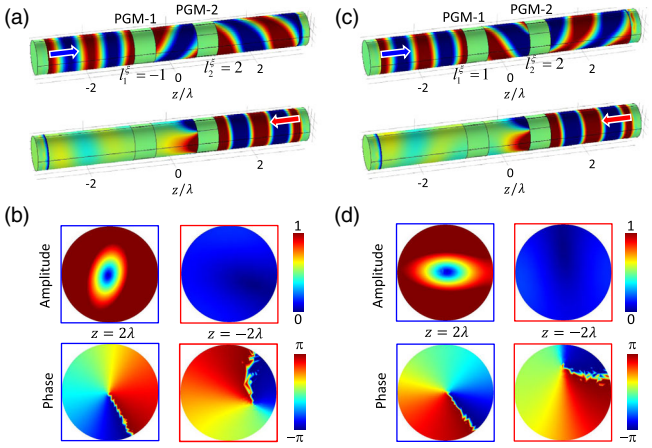

FIG. 3. Numerical demonstration for asymmetric generation of acoustic vortex. The simulated total field patterns of an incident plane wave from the left (upper) and right (lower) sides of the waveguide for the PGMs with the opposite (a) and the same (c) helicity. The corresponding amplitude and phase on the transmitted sides of the left and right incidences for the PGMs with the opposite (b) and the same (d) helicity.

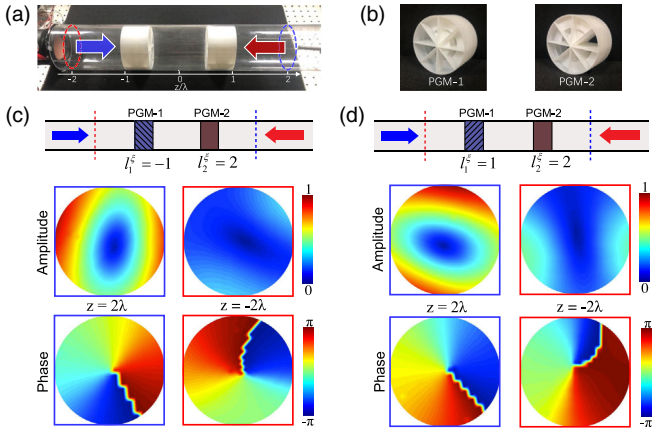

FIG. 4. Experimental demonstration for asymmetric generation of acoustic vortex. (a) Experimental setup. (b) Fabricated samples. (c) and (d) are experimentally measured phase and amplitude distributions at $z = \pm 2\lambda$ of the waveguide for the PGMs with the opposite and the same helicity. The measured field is normalized to the acoustic field at the same distance in an empty waveguide.

back by the PGM-2. Because of the imperfect design of the PGM structures (92% transmission in one cell is lower than these in others with the average transmission of 98.3% [37]), some weak waves mainly composed of $l = 0$ leak out from the PGM-2, and it is twisted by the PGM-1 into a weak vortex with $l^t = 1$. The asymmetric generation of acoustic vortex is seen from the corresponding amplitude and phase on the transmitted sides ($z = \pm 2\lambda$) for both incidences in Fig. 3(b). The high-efficiency acoustic vortex with $l^t = 1$ for the left incidence is revealed from the high amplitude with null core and the perfect spiral phase distribution at the cross section of $z = 2\lambda$. While for the right incidence, the weak amplitude and the imperfect spiral phase are found at $z = -2\lambda$, implying that a low-efficiency and imperfect acoustic vortex is generated. The imperfect phase profile of $l^t = 1$ is mainly caused by other weak vortex or guided modes in the waveguide. We numerically calculate the transmission efficiencies (square root of the outgoing to incoming sound power) as 98.1% and 5.9% for the left and right incidences, respectively, which quantitatively shows the one-way performance of the vortex generation, even though the designed PGMs are not so perfect and a few unit cells are used. Similar results are also found for the designed metasurfaces with the same helicity. As shown in Fig. 3(c), a strong vortex with $l^t = -1$ is generated for the left incidence, and it is a weak and imperfect vortex with $l^t = -1$ for the right incidence. These results are revealed by the corresponding phase and amplitude on the transmitted sides [see Fig. 3(d)]. Their transmission efficiencies of the left and right incidences are numerically calculated as 92.9% and 6.1%, respectively. Therefore, numerical simulations confirm the proposed asymmetric generation of acoustic vortex.

Experiments to verify the asymmetric generation of acoustic vortex are conducted in a cylindrical waveguide with two PGMs, as shown in Fig. 4(a). The metasurfaces are fabricated by 3D printing with commercial photopolymer materials [see Fig. 4(b)], which can be regarded as impenetrable for airborne acoustics. The fabricated metasurfaces are placed in the cylindrical waveguide with a diameter of 8.0 cm and the distance between two PGMs is 10.0 cm. In experiments, the incident plane wave is generated by a speaker (HiVi M3N). The transmitted field is scanned using a moving acoustic pressure probe (Brüel & Kjær 4939 0.25-in microphone) with a step of 2.0 mm. Because of the limitation of the experimental conditions inside the waveguide, the overall scanning area is slightly smaller than the cross section of the tube, which is 4.8×4.8 cm. The scanning area is operated at the position of $z = \pm 2\lambda$ in the waveguide. For the metasurfaces placed with the opposite helicity, the experimentally measured phase and amplitude distributions for both incidences are shown in Fig. 4(c). A strong vortex with $l^t = 1$ is generated for the left incidence, and while a weak vortex with $l^t = 1$ occurs for the right incidence. For the metasurfaces with the same helicity, the asymmetric generation of acoustic vortex with $l^t = -1$ is also realized [see Fig. 4(d)]. The experimentally measured amplitude and phase of the transmitted vortices slightly deviate from these in simulations, which is mainly caused by the intrinsic losses in the PGMs and fabrication errors. We numerically introduce empirical losses in the air areas of the PGMs to mimic the viscous and thermal dissipation, and the corresponding simulated results [37] are almost consistent with the experimental ones. Furthermore, we numerically calculate the corresponding transmission efficiencies of the left and right

incidences for the lossy metasurfaces with the opposite (same) helicity as 60.6% and 15.1% (40.1% and 6.1%), respectively. The transmission efficiency of the left incidence in the case of the same helicity is lower than that in the opposite one, which results from multiple internal reflections in the PGM-2 that bring more absorption. All in all, even considering the effect of losses, asymmetric generation of acoustic vortex via the dual-layer metasurfaces is numerically and experimentally demonstrated.

In conclusion, by involving the dual-layer metasurfaces in a cylindrical waveguide, we have numerically and experimentally demonstrated the asymmetric generation of acoustic vortex. Based on the vortex diffraction rule of a single PGM [33], a general scheme developed from both ITC and ETC in the dual-layer PGMs has been proposed for this novel asymmetric effect. Beyond showing the asymmetric generation of the first-order acoustic vortex in our experiments, the proposed approach can be applied to the case of higher-order acoustic vortex [37]. Our work, therefore, provides a feasible way to realize asymmetric generation for acoustic OAM, which can enrich the study of acoustic OAM and might have asymmetric applications in particle manipulation [41] and OAM-based communications [42]. For example, one-way OAM-based communications could be potentially used in intelligence communication to protect the instruction publisher. Our findings are essentially general wave physics, and therefore could be extended to other types of waveguides, such as optical fibers [43,44].

This work was supported by the National Natural Science Foundation of China (Grants No. 11904169 and No. 11974010), the Natural Science Foundation of Jiangsu Province (Grant No. BK20190383), the Postdoctoral Science Foundation of Jiangsu Province (Grant No. 2020Z224), the Postdoctoral Science Foundation of China (Grant No. 2020M681576), Top-notch Academic Programs Project of Jiangsu Higher Education Institutions, and Priority Academic Program Development of Jiangsu Higher Education Institutions. Y. T., S. Y., and M.-H. L. acknowledge support from the National Key R&D Program of China (Grants No. 2017YFA0303702 and No. 2018YFA0306200).

Y. F., Y. T., and X. L. contributed equally to this work.

*yyfu@nuaa.edu.cn
†ydxu@suda.edu.cn
‡luminghui@nju.edu.cn

[1] K. Fang, Z. Yu, and S. Fan, Realizing effective magnetic field for photons by controlling the phase of dynamic modulation, Nat. Photonics **6**, 782 (2012).

[2] B. Liang, B. Yuan, and J.-C. Cheng, Acoustic Diode: Rectification of Acoustic Energy Flux in One-Dimensional Systems, Phys. Rev. Lett. **103**, 104301 (2009).

[3] X. Li, X. Ni, L. Feng, M. Lu, C. He, and Y. F. Chen, Tunable Unidirectional Sound Propagation through a Sonic Crystal-Based Acoustic Diode, Phys. Rev. Lett. **106**, 084301 (2011).

[4] Y. Xu, C. Gu, B. Hou, Y. Lai, J. Li, and H. Chen, Broadband asymmetric waveguiding of light without polarization limitations, Nat. Commun. **4**, 2561 (2013).

[5] Z. Wang, Y. Chong, J. D. Joannopoulos, and M. Soljačić, Observation of unidirectional backscattering-immune topological electromagnetic states, Nature (London) **461**, 772 (2009).

[6] Z. Yu and S. Fan, Complete optical isolation created by indirect interband photonic transitions, Nat. Photonics **3**, 91 (2009).

[7] B. Liang, X. Guo, J. Tu, D. Zhang, and J. Cheng, An acoustic rectifier, Nat. Mater. **9**, 989 (2010).

[8] Z. Lin, H. Ramezani, T. Eichelkraut, T. Kottos, H. Cao, and D. N. Christodoulides, Unidirectional Invisibility Induced by *PT*-Symmetric Periodic Structures, Phys. Rev. Lett. **106**, 213901 (2011).

[9] L. Feng, Y. L. Xu, W. S. Fegadolli, M. H. Lu, J. E. B. Oliveira, V. R. Almeida, Y. F. Chen, and A. Scherer, Experimental demonstration of a unidirectional reflectionless parity-time metamaterial at optical frequencies, Nat. Mater. **12**, 108 (2013).

[10] C. He, X. Ni, H. Ge, X. Sun, Y. Chen, M. Lu, X. Liu, and Y. Chen, Acoustic topological insulator and robust one-way sound transport, Nat. Phys. **12**, 1124 (2016).

[11] Y. Yang, Y. Xu, T. Xu, H. Wang, J. Jiang, X. Hu, and Z. Hang, Visualization of a Unidirectional Electromagnetic Waveguide Using Topological Photonic Crystals Made of Dielectric Materials, Phys. Rev. Lett. **120**, 217401 (2018).

[12] C. Pfeiffer, C. Zhang, V. Ray, L. Guo, and A. Grbic, High Performance Bianisotropic Metasurfaces: Asymmetric Transmission of Light, Phys. Rev. Lett. **113**, 023902 (2014).

[13] D. Frese, Q. Wei, Y. Wang, L. Huang, and T. Zentgraf, Nonreciprocal asymmetric polarization encryption by layered plasmonic metasurfaces, Nano Lett. **19**, 3976 (2019).

[14] X. C. Wang, A. Díaz-Rubio, V. S. Asadchy, G. Ptitcyn, A. A. Generalov, J. Ala-Laurinaho, and S. A. Tretyakov, Extreme Asymmetry in Metasurfaces via Evanescent Fields Engineering: Angular-Asymmetric Absorption, Phys. Rev. Lett. **121**, 256802 (2018).

[15] Y. Fu, J. Tao, A. Song, Y. Liu, and Y. Xu, Controllably asymmetric beam splitting via gap-induced diffraction channel transition in dual-layer binary metagratings, Front. Phys. **15**, 52502 (2020).

[16] L. Feng, M. Ayache, J. Huang, Y. Xu, M. Lu, Y. Chen, Y. Fainman, and A. Scherer, Nonreciprocal light propagation in a silicon photonic circuit, Science **333**, 729 (2011).

[17] Y. Cao, Y. Fu, Q. Zhou, X. Ou, L. Gao, H. Chen, and Y. Xu, Mechanism behind Angularly Asymmetric Diffraction in Phase-Gradient Metasurfaces, Phys. Rev. Applied **12**, 024006 (2019).

[18] W. Wang, L. Wang, R. Xue, H. Chen, R. Guo, Y. Liu, and J. Chen, Unidirectional Excitation of Radiative-Loss-Free Surface Plasmon Polaritons in PT -Symmetric Systems, Phys. Rev. Lett. **119**, 077401 (2017).

[19] Y. Shen, X. Wang, Z. Xie, C. Min, X. Fu, Q. Liu, M. Gong, and X. Yuan, Optical vortices 30 years on: OAM manipulation from topological charge to multiple singularities, Light Sci. Appl. **8**, 90 (2019).

[20] M. Padgett and R. Bowman, Tweezers with a twist, Nat. Photonics **5**, 343 (2011).
[21] M. Baudoin, J.-C. Gerbedoen, A. Riaud, O. B. Matar, N. Smagin, and J.-L. Thomas, Folding a focalized acoustical vortex on a flat holographic transducer: Miniaturized selective acoustical tweezers, Sci. Adv. **5**, eaav1967 (2019).
[22] C. Zhang, C. Min, L. Du, and X.-C. Yuan, Perfect optical vortex enhanced surface plasmon excitation for plasmonic structured illumination microscopy imaging, Appl. Phys. Lett. **108**, 201601 (2016).
[23] J. Wang, J. Yang, I. M. Fazal, N. Ahmed, Y. Yan, H. Huang, Y. Ren, Y. Yue, S. Dolinar, M. Tur, and A. E. Willner, Terabit free-space data transmission employing orbital angular momentum multiplexing, Nat. Photonics **6**, 488 (2012).
[24] C. Shi, M. Dubois, Y. Wang, and X. Zhang, High-speed acoustic communication by multiplexing orbital angular momentum, Proc. Natl. Acad. Sci. U.S.A. **114**, 7250 (2017).
[25] X. Wang, Z. Nie, Y. Liang, J. Wang, T. Li, and B. Jia, Recent advances on optical vortex generation, Nanophotonics **7**, 1533 (2018).
[26] M. L. N. Chen, L. J. Jiang, and W. E. Sha, Orbital angular momentum generation and detection by geometric-phase based metasurfaces, Appl. Sci. **8**, 362 (2018).
[27] X. Jiang, Y. Li, B. Liang, J. Cheng, and L. Zhang, Convert Acoustic Resonances to Orbital Angular Momentum, Phys. Rev. Lett. **117**, 034301 (2016).
[28] H. Esfahlani and H. Lissek, Generation of acoustic helical wavefronts using metasurfaces, Phys. Rev. B **95**, 024312 (2017).
[29] Z. Guo, H. Liu, H. Zhou, K. Zhou, S. Wang, F. Shen, Y. Gong, J. Gao, S. Liu, and K. Guo, High-order acoustic vortex field generation based on a metasurface, Phys. Rev. E **100**, 053315 (2019).
[30] S. Fan, Y. Wang, L. Cao, Y. Zhu, A. Chen, B. Vincent, B. Assouar, and Y. Wang, Acoustic vortices with high-order orbital angular momentum by a continuously tunable metasurface, Appl. Phys. Lett. **116**, 163504 (2020).
[31] C. Liu, H. Long, C. Ma, Y. Jia, C. Shao, Y. Cheng, and X. Liu, Broadband acoustic vortex beam generator based on coupled resonances, Appl. Phys. Lett. **118**, 143503 (2021).
[32] S. Gao, Y. Li, C. Ma, Y. Cheng, and X. Liu, Emitting long-distance spiral airborne sound using low-profile planar acoustic antenna, Nat. Commun. **12**, 2006 (2021).
[33] Y. Fu, C. Shen, X. Zhu, J. Li, Y. Liu, S. A. Cummer, and Y. Xu, Sound vortex diffraction via topological charge in phase gradient metagratings, Sci. Adv. **6**, eaba9876 (2020).
[34] Y. Li, C. Shen, Y. B. Xie, J. F. Li, W. Q. Wang, S. A. Cummer, and Y. Jing, Tunable Asymmetric Transmission via Lossy Acoustic Metasurfaces, Phys. Rev. Lett. **119**, 035501 (2017).
[35] C. Shen and S. A. Cummer, Harnessing Multiple Internal Reflections to Design Highly Absorptive Acoustic Metasurfaces, Phys. Rev. Applied **9**, 054009 (2018).
[36] Y. Fu, C. Shen, Y. Cao, L. Gao, H. Chen, C. T. Chan, S. A. Cummer, and Y. Xu, Reversal of transmission and reflection based on acoustic metagratings with integer parity design, Nat. Commun. **10**, 2326 (2019).
[37] See Supplemental Material at http://link.aps.org/supplemental/10.1103/PhysRevLett.128.104501 for details on the simulated results for PGM-2 with robust ETC, vortex generation in the waveguide with dual-layer spiral phase plates, PGM design, asymmetric vortex generation in lossy PGMs, and asymmetric higher-order vortex generation.
[38] Z. Liang and J. Li, Extreme Acoustic Metamaterial by Coiling Up Space, Phys. Rev. Lett. **108**, 114301 (2012).
[39] J. Xia, X. Zhang, H. Sun, S. Yuan, J. Qian, and Y. Ge, Broadband Tunable Acoustic Asymmetric Focusing Lens from Dual-Layer Metasurfaces, Phys. Rev. Applied **10**, 014016 (2018).
[40] L. Cao, Y. Xu, B. Assouar, and Z. Yang, Asymmetric flexural wave transmission based on dual-layer elastic gradient metasurfaces, Appl. Phys. Lett. **113**, 183506 (2018).
[41] L. Ye, C. Qiu, J. Lu, K. Tang, H. Jia, M. Ke, S. Peng, and Z. Liu, Making sound vortices by metasurfaces, AIP Adv. **6**, 085007 (2016).
[42] X. Jiang, B. Liang, J. C. Cheng, and C. W. Qiu, Twisted acoustics: Metasurface-enabled multiplexing and demultiplexing, Adv. Mater. **30**, 1800257 (2018).
[43] G. Wong, M. Kang, H. Lee, F. Biancalana, C. Conti, T. Weiss, and P. St. J. Russell, Excitation of orbital angular momentum resonances in helically twisted photonic crystal fiber, Science **337**, 446 (2012).
[44] P. Gregg, P. Kristensen, and S. Ramachandran, Conservation of orbital angular momentum in air-core optical fibers, Optica **2**, 267 (2015).